Science
AAAS

RESEARCH ARTICLES

Morphology and Composition of the Surface of Mars: Mars Odyssey THEMIS Results

Philip R. Christensen,[1]* Joshua L. Bandfield,[1] James F. Bell III,[2] Noel Gorelick,[1] Victoria E. Hamilton,[3] Anton Ivanov,[4] Bruce M. Jakosky,[5] Hugh H. Kieffer,[6] Melissa D. Lane,[7] Michael C. Malin,[8] Timothy McConnochie,[2] Alfred S. McEwen,[9] Harry Y. McSween Jr.,[10] Greg L. Mehall,[1] Jeffery E. Moersch,[10] Kenneth H. Nealson,[11] James W. Rice Jr.,[1] Mark I. Richardson,[12] Steven W. Ruff,[1] Michael D. Smith,[13] Timothy N. Titus,[6] Michael B. Wyatt[1]

The Thermal Emission Imaging System (THEMIS) on Mars Odyssey has produced infrared to visible wavelength images of the martian surface that show lithologically distinct layers with variable thickness, implying temporal changes in the processes or environments during or after their formation. Kilometer-scale exposures of bedrock are observed; elsewhere airfall dust completely mantles the surface over thousands of square kilometers. Mars has compositional variations at 100-meter scales, for example, an exposure of olivine-rich basalt in the walls of Ganges Chasma. Thermally distinct ejecta facies occur around some craters with variations associated with crater age. Polar observations have identified temporal patches of water frost in the north polar cap. No thermal signatures associated with endogenic heat sources have been identified.

THEMIS began observing the surface and atmosphere of Mars in February 2002 with the use of thermal infrared (IR) multispectral imaging between 6.5 and 15 μm and visible to near-IR images from 450 to 850 nm (*1*). The unique aspect of this investigation is images of martian temperatures at a resolution of 100 m. The temperatures are related to material properties, such as composition and structural integrity, climate and topography, which in turn are indications of the origin, evolution, and history of the planet [see supporting online material (SOM) Text]. Daytime thermal images incorporate the effects of surface emissivity, reflectance, thermal properties, and slope, whereas nighttime thermal images show predominantly the effects of intrinsic thermal properties. The investigation objectives are to: (i) determine the mineralogy of localized deposits, including hydrothermal or subaqueous environments; (ii) search for thermal anomalies associated with active subsurface hydrothermal systems; (iii) study 100-m scale processes and landing site characteristics using morphologic and thermophysical properties; and (iv) investigate polar cap processes.

Thermophysical properties of layered units. A major result from Mars Global Surveyor (MGS) imaging was the discovery of rock units that are layered at meter to tens of meter scales (*2*, *3*). A major result from the THEMIS IR camera is the discovery that the physical and compositional properties of these layers can vary, implying temporal changes in the processes or environments that formed the different units. A key element of this discovery is the exposure at the surface of materials that directly reflect the properties of the underlying rock unit from which they were derived.

Some of the best examples of thermally distinct units occur in Terra Meridiani (Fig. 1) (*4*). These units vary from kilometer-scale deposits within 5- to 50-km-diameter craters, to regional layered surfaces extending tens to hundreds of kilometers. Isolated outliers with similar thermal characteristics may be erosional remnants of once-continuous layers. Temperature contrast reversals from day to night (Fig. 1; fig. S1) indicate that the primary differences are due to differences in thermal inertia (SOM Text) (*5*, *6*).

Eight thermal inertia units (A to H) have been identified (Fig. 1). Units A, C, E, and F are extensive enough (> 50 km by 50 km in size) to be well characterized in Thermal Emission Spectrometer (TES) global thermal inertia maps (*7*). The TES-derived values of thermal inertia (**I**) for units A, C, E, and F are 280 to 340, 530 to 580, 330 to 360, and 340 to 350 J m^{-2} sec$^{-1/2}$ K^{-1}, respectively (physical units of **I** are omitted hereafter). Thermal inertia mapping of coherent units that are below the size resolvable by TES can be accomplished by modeling temperature differences relative to the temperature of materials of known inertia (*6–8*). These models show that the thermal inertia of the small Meridiani units are: Unit B, 350 to 400; Unit D, ~450; Unit G, ~375; and Unit H, ~550. Units A, C, and F are widespread and correspond to units mapped as "Plains" (P), "Etched" (E), and "Dissected Crater Terrain" (DCT), respectively (*9*).

Unit B (Fig. 2) is rich in crystalline hematite (*10*). It is thermally distinct from the surface on which it was deposited, and it shows layering, muted craters, and an erosional pattern suggestive of loosely consolidated material. Stratigraphic relations observed in the THEMIS images show that Unit B is on top of Unit C, which is on top of Unit F (Fig. 1). To the west, a sequence has been exposed by erosion, revealing a sequence stratigraphically downward from Unit C to Unit E (Fig. 1).

If we assume that the surface materials reflect the particle size distribution of the underlying unit from which they were derived (i.e., no winnowing or concentration has occurred) and are unconsolidated to a depth of several diurnal thermal skin depths (~5 to 20 cm), then the average particle size of the units in Meridiani range from ~1 mm for the lowest inertia units to ~1 cm for the high-inertia units (*11*). Alternatively, the differences in inertia can be caused by the abundance of larger rocks or blocky debris weathered from the different units. Assuming a constant **I** = 300 for fine-grained material and **I** = 1200 for blocks (*12*), the block abundances would range from 0 (lowest **I**) to 30% (highest **I**) for the Meridiani units.

The exposure of different layers within the stratigraphic section, together with the existence of outliers of once-continuous units, indicates that extensive erosion occurred within the Meridiani region after the initial deposition of the different rock units. In addition, the differences in the physical properties of these units indicate that there were changes in processes or environ-

[1]Department of Geological Sciences, Arizona State University, Tempe, AZ 85287–6305, USA. [2]Department of Astronomy, Cornell University, Ithaca, NY 14853–6801, USA. [3]Hawaii Institute of Geophysics and Planetology, University of Hawaii, Honolulu, HI 96822, USA. [4]Jet Propulsion Laboratory, Pasadena, CA 91109–8099, USA. [5]LASP, University of Colorado, Boulder, CO 80309, USA. [6]U.S. Geological Survey, Flagstaff, AZ 86001, USA. [7]Planetary Science Institute, Phoenix, AZ 85032, USA. [8]Malin Space Science Systems, San Diego, CA 92191–0148, USA. [9]Lunar and Planetary Lab, University of Arizona, Tucson, AZ 85721, USA. [10]Department of Geological Sciences, University of Tennessee, Knoxville, TN 37996–1410, USA. [11]University of Southern California, Los Angeles, CA 90089, USA. [12]Division of Geological and Planetary Sciences, California Institute of Technology, Pasadena, CA 91125, USA. [13]Goddard Space Flight Center, Greenbelt, MD 20771, USA.

*To whom correspondence should be addressed. E-mail: phil.christensen@asu.edu

ments during or after their emplacement. Likely causes are: (i) differences in density and porosity between igneous and clastic sedimentary materials or among igneous materials, (ii) variations in particle size and sorting among different sedimentary deposits, and (iii) variations in the degree of lithification or cementation among initially similar clastic or pyroclastic materials. Igneous flows, intrusive bodies, or welded tephra deposits have a relatively high I due to high density and thermal conductivity, whereas some pyroclastic deposits (particularly airfall units) have relatively low I. No obvious volcanic flow textures or vent structures are visible in this region, although ridge morphologies commonly associated with compression in volcanic plains are apparent on Unit F. Mars has a variety of sedimentary deposits, including those associated with impact cratering, catastrophic floods, debris flows, landslides, and aeolian traction, saltation, and suspension. Differences in sediment supply, entrainment, or deposition in such flows could result in clastic sediments that range in particle size from meters to micrometers, which would then be represented by changes in the physical properties of deposits. Finally, the rhythmic variation in the competency of layered sedimentary rocks (2, 3) indicates that variations in the degree of lithification by burial or cementation by pore-circulating fluids have occurred. The Meridiani units may have been compacted beneath a kilometer or more of overburden that has since been removed (13). Cementation by subsurface aqueous fluids has been proposed to explain both observed hematite mineralization (10) and secondary mineralization in the martian meteorites (e.g., 14).

Rocks and bedrock. THEMIS infrared images have revealed the occurrence of kilometer-scale outcrops of exposed bedrock. The floor of the Nili Patera caldera (9°N, 67°E) has nighttime surface brightness temperatures of 215 to 217 K over an ~30 km² area (Fig. 3). Thermal models using the appropriate local time (3.25 hours; 24 hours equal one martian day), season [aerocentric longitude (Ls) 333.5°, orbit 903], location, elevation (0.2 km), and infrared dust opacity (0.15) predict temperatures of 218 K for a thermal inertia corresponding to solid rock ($I = 2200$), indicating that these portions of the caldera floor are exposed bedrock. Dark barchan dunes, which form through sand transport across a hard surface where a source of sand is limited, are superimposed on this bedrock surface (fig. S2). Sand transport across this region may have stripped away fine-grained particles to expose the bedrock surface. The temperature of the dunes is 192 ± 1 K, corresponding to $I = $ ~400. This inertia equates to an average grain size of >1 mm (11); alternatively, these dunes may be finer-grained, inactive sand that is slightly crusted or indurated.

Rock surfaces are also observed near the mouth of Ares Valles (~22°N, ~324°E) about 250 km downstream of the Pathfinder

Fig. 1. Mosaic of temperature images of Terra Meridiani. Mosaic covers the region from 2°S to 6°N, 352° to 360°E; north is toward the top. The individual image strips are ~32 km wide with 100 m per pixel resolution. The calibrated radiance in each strip was normalized to reduce changes due to the local time variation of the Odyssey orbit. Dark regions are cooler, bright regions are warmer in each mosaic. The letters indicate locations or units discussed in the text; e.g., hematite-rich Unit B is stratigraphically above Unit C (Etched Terrain), which is above Unit F (Dissected Crater Terrain). The inset shows the full resolution of the region outlined by the small box. This is a mosaic of nighttime temperature images, when small variations of thermophysical properties are significantly more visible. Bright (warm) areas have higher thermal inertia. Normalized temperatures vary from approximately 165 to 200 K. The extensive ejecta of the 20-km-diameter crater near the center indicates that it is relatively young. Dashed box indicates location of Fig. 2.
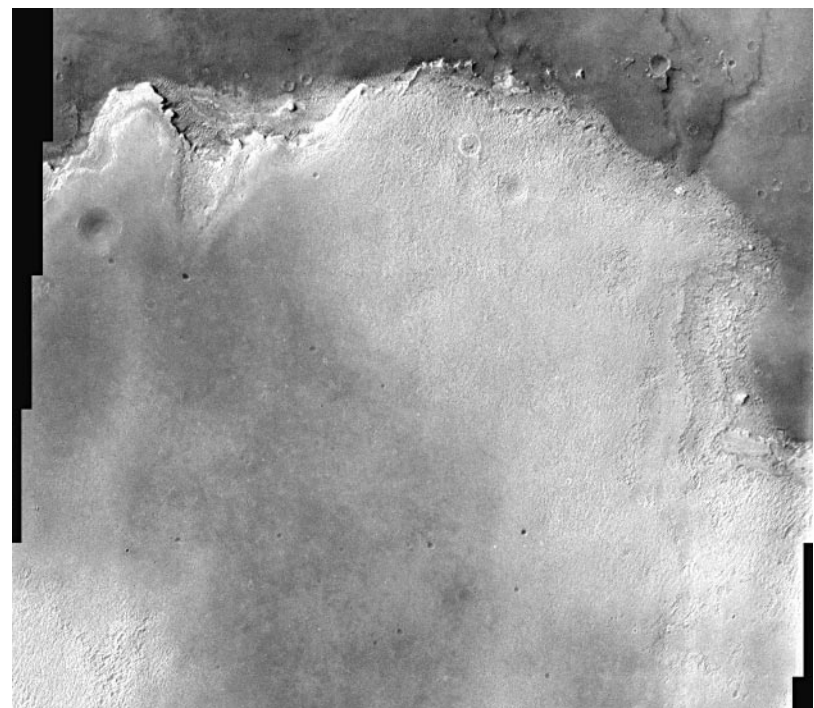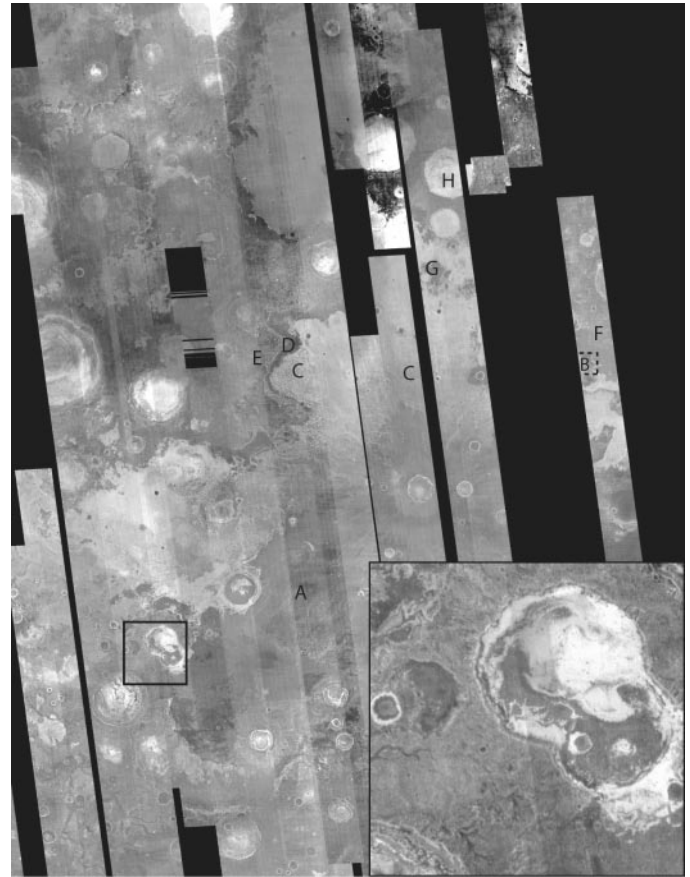

Fig. 2. THEMIS visible image of area indicated by dashed box in Fig. 1, showing the layering of this hematite-bearing unit and illustrating the detail observed at the full 18 m per pixel resolution of the visible imager.

landing site (Fig. 4). Day-night temperature contrast reversals show a wide range of thermophysical properties in this region that correlate with morphologic units. The warmest nighttime temperatures are ~207 K, consistent with exposed rock. Both of the ~8-km-diameter craters in the image have hummocky and rayed ejecta, with the rays extending two to three crater diameters from the rim. The nighttime temperatures of these deposits (191 to 193 K) show that they consist of disaggregated material with an average particle size of ≥1 mm. The preservation of the fine-grained ejecta, including the details of individual rays, on top of the bedrock indicates that the processes that exposed the bedrock occurred before the ejecta emplacement and have not been active since the impact.

Nighttime IR images commonly show elevated temperatures on the slopes of canyons, craters, mesas, channels, and fissures (fig. S3). Slopes are typically 5 to 15 K warmer than the surroundings, independent of slope azimuth, and occur on the walls of closed and open depressions (SOM Text). There is no evidence of endogenic heat, even in isolated cases such as the relatively young volcanic fissures in South Elysium (15). We conclude that the higher slope temperatures are due to a concentration of coarse (warm) material on slopes relative to the surrounding flat-lying surfaces. Concentrations of 10 to 35% rocks (12, 16) are required to produce the observed slope temperatures.
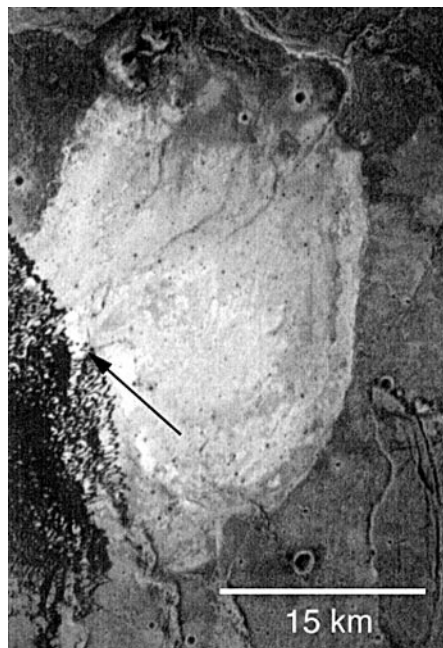
The presence of rocky material on martian slopes indicates that the production or exposure rate of blocks or in situ rock layers on slopes is greater than the rate of burial and/or weathering and erosion. Currently the most prevalent form of burial on Mars is fallout of airborne dust. Several factors may reduce the amount of burial on slopes: Dust may be removed in occasional catastrophic dust flows (17) or downslope movement of rocks; Air turbulence over blocky material may prevent dust from settling; or, once settled, Turbulence may enhance the remobilization of dust during periods of higher wind. Together these processes prevent net dust accumulation to a thickness greater than the size of the blocky materials [>~30 cm (16)].

Rocks are also detected in THEMIS temperature images around numerous impact craters. Ejecta often have distinctive concentric temperature patterns and generally are relatively cool in daytime IR and warm in nighttime IR images (fig. S4). Coarse-grained ejecta are observed around craters varying in size from the limit of detection (~0.5 km diameter) to craters tens of kilometers in diameter. Observed patterns range from rays of blocky material radiating outward up to 8 to 10 crater diameters from the crater rim, (fig. S4, A to C) to halos of coarse material extending 1 to 2 crater diameters (fig. S4, D to

F). In some cases (Fig. S4, A and C) there is an outer annulus of material that is finer grained than the surrounding surface, which transitions to coarser material close to the crater rim. Flow-ejecta craters (18, 19) can exhibit several distinct thermal inertia boundaries between different lobes, suggesting differences in the processes of ejecta emplacement or modification (fig. S4, D to F). Within a given region, not all craters of similar size or degree of degradation have thermally distinct ejecta (fig. S4, A, C, and F), nor is there a clear dependence of ejecta thermal pattern on crater size. These variations in the character of ejecta surfaces of similar-sized craters over short (kilometer-scale) distances may be due to differences in crater age (20).

Massive landslides have dropped ~7.5 km off of the northern wall of western Melas Chasma in Valles Marineris (~8°S; ~282°E), exposing a layer several hundred meters thick ~0.5 km below the canyon rim that is warm (blocky) in nighttime IR images. The landslide deposits have temperature variations of 10 to 12 K that delineate differences in the physical properties of individual longitudinal and transverse ridges and grooves spaced 0.5 to 1 km apart that formed during the landslide process. The temperature varies in the groove or ridge surfaces from ~186 to ~198 K, which represents a factor of three to five difference in

Fig. 3. Nighttime temperature of Nili Patera. THEMIS image I00903005, centered near 8.5°N, 67.5°E, covering an area ~32 km wide. Temperatures range from 191.4 K (dark) to 216.5 K (white). The highest temperature areas are exposed rock. The arrow indicates region of dunes seen in fig. S2.

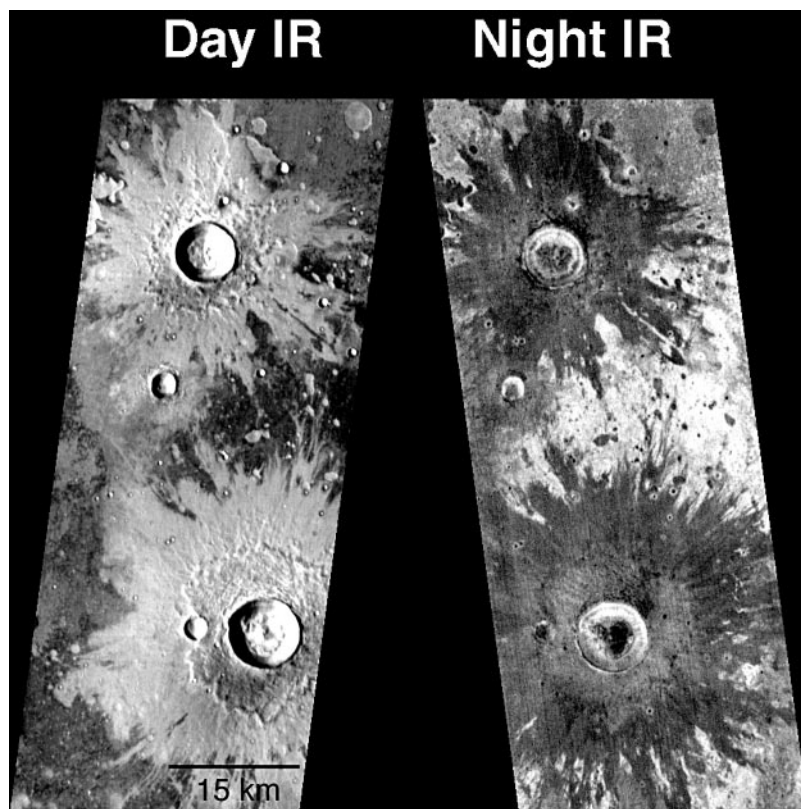Fig. 4. Day-night IR image pair of craters in Chryse basin near 22.5°N, 324°E. Daytime image is I02685009; nighttime image is I01980010. The relative tilt in the images is due to the inclination of the orbit track on the ascending (night) and descending (day) portion of the orbit. Nighttime temperatures range from 187.8 K (dark) to 203.7 K (white); daytime temperatures range from 232.5 K to 248.5 K.

average particle size or a variation in surface rock abundance from 0 to 30%.

Mobile surface materials: sand and dust. Nighttime images of large dune fields can resolve individual dunes, revealing particle size differences between the dune and interdune surfaces and between the dune fields and the surrounding terrain (Fig. 5). Dunes in Russell crater (Fig. 5) are coarser-grained (warmer at night) than the interdune surfaces, possibly due to the accumulation of airfall dust in interdune regions where active sand motion may be limited. Conversely, the dunes in Kaiser crater are generally finer-grained than their surroundings, which include localized regions of bedrock, suggesting accumulation of sand on top of a rocky substrate. The thermal inertia of dunes in both regions is 500 to 600. If these dunes are composed of unconsolidated sand, they have average grain sizes of several millimeters or greater; alternatively, they may be finer-grained, inactive sand that has been slightly indurated.

Previous low-resolution (3 to 5 km) infrared mapping of Mars has shown extensive dust mantles from 1 to 3 m thick centered on the Tharsis volcanic province and the ancient cratered terrain in Arabia Terra (6–8, 21, 22). Nighttime IR images show that these dust mantles are continuous at 100-m spatial scales, with no evidence of rocky ridges or rubble-covered flow boundaries protruding through the dust over thousands of square kilometers of lava flow fields. Nighttime temperatures on the flanks of the Olympus Mons volcano are near 155 K, corresponding to a thermal inertia <150 (average particle size <~40 μm), and vary by less than 2 K over thousands of square kilometers. The homogeneity of this mantle at 100-m spatial scales indicates that dust settles uniformly from the atmosphere and has not been disturbed and redistributed by the wind to expose rocky prominences and flow fronts, resulting in a thin dust blanket uniformly draping the landscape.

Compositional variations. TES hyperspectral data have been used to map the mineralogy of martian surface materials at 5-km spatial scales (10, 23–25), but cannot resolve individual units at scales appropriate to specific formation processes, e.g., lava flows and sedimentary layers. THEMIS multispectral infrared images have a factor of 1500 improvement in areal resolution over TES, producing compositional maps at the scales of individual lithologic units. THEMIS data have identified a spectrally distinct unit that crops out as east-west trending bands in the lower walls of the Ganges Chasma outlet canyon (Fig. 6). This unit occurs within 50 m of the same elevation on both sides of the canyon and is exposed on a bench surrounding a low knob on the canyon floor. The outcrop pattern indicates that this unit is a layer within the canyon wall sequence, rather
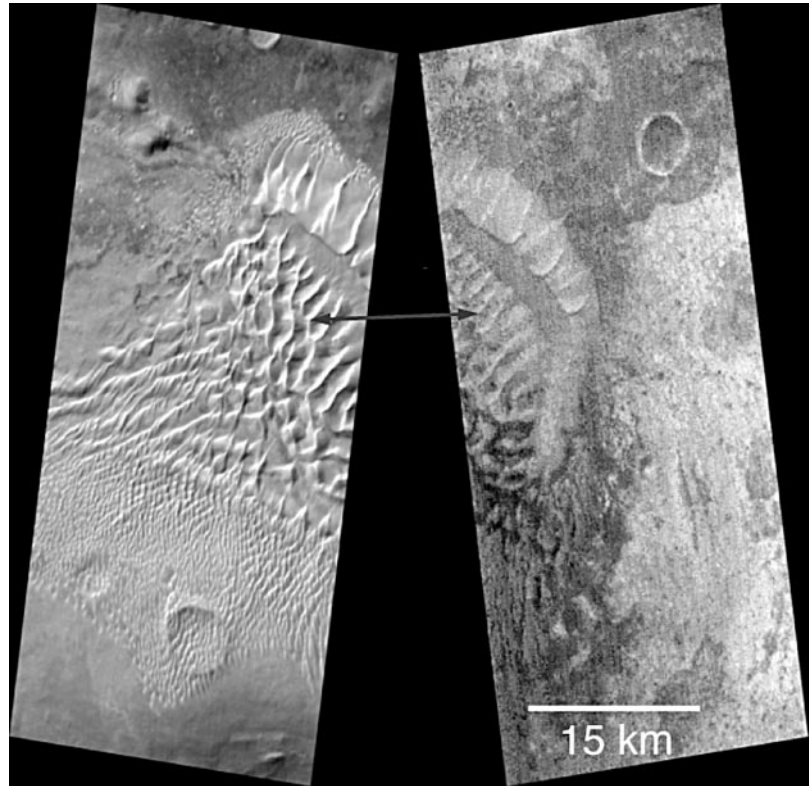

Fig. 5. Day-night image pair of the Russell crater (54°S; 13°E) dune field. The temperatures range from approximately 240 to 260 K in the day and 170 to 190 K at night. Arrows connect common locations seen in each image. The relative tilt in the images is due to the inclination of the orbit track on the ascending (night; THEMIS image I01417005) and descending (day; THEMIS image I00824002) portion of the orbit.
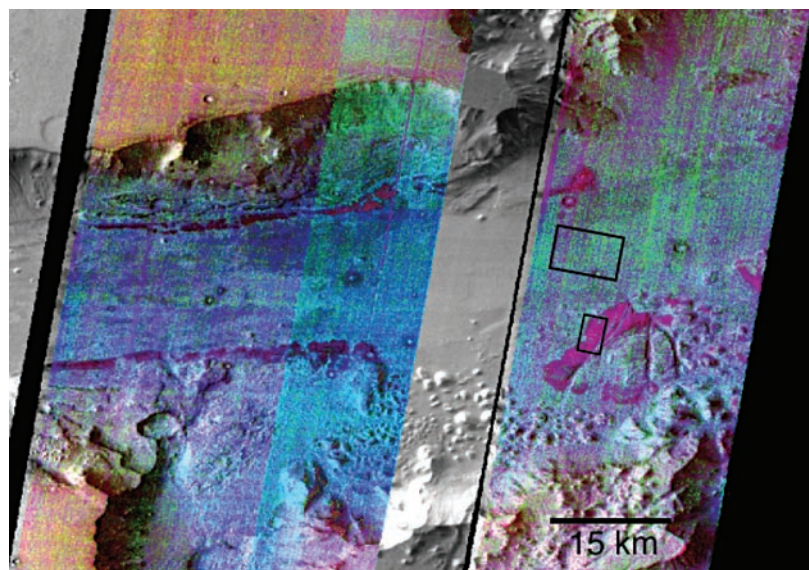

Fig. 6. Color infrared image mosaic of Ganges Chasma. This false-color mosaic of three images was created using a decorrelation stretch (32) of the calibrated radiance from bands 5 (centered at 9.35 μm), 7 (11.04 μm), and 8 (11.79 μm). Orange-colored material on plateaus is dust; blue-colored material on canyon floor is determined from TES to be basalt; purple-colored bands trending east-west are olivine-rich basalt. Monochrome image strips are single-band THEMIS temperature images where multispectral data is not available. Boxes show location of the individual TES spectra used to create spectral ratio shown in fig. S5. No inter-image adjustments nor atmospheric corrections have been applied. North is toward the top.

2059

than a surficial deposit. The nighttime temperature (204 K; $I = 700$) is ~10 K higher than the surrounding material, indicating that this layer is blockier than its surroundings. The composition of the Ganges floor material is determined from TES data to be basaltic. The difference in composition between the wall layer and floor material was determined using a ratio of TES spectra of the floor and wall unit (fig. S5) (*26*) to be olivine with an Mg/(Mg+Fe) ratio of 68 (Fo$_{68}$) at an abundance of 10 to 15%. This example illustrates how THEMIS and TES data will be combined to determine the composition of small-scale units, in this case less than one TES pixel (3 km by 5 km) in size, and place them in their geologic context.

This layer of olivine-rich basalt is 50 to 100 m thick, occurs beneath 4.5 km of overlying rocks, and extends over an area at least 30 km by 100 km in size. It was most likely emplaced as an olivine-enriched lava flow, followed by 4.5 km of overlying units; injected as sill; or formed as a cumulate layer in layered intrusive body. Alternatively, it could be a sedimentary layer in which olivine was enriched during transport or deposition. This layer was once buried to a depth of at least 4.5 km. The preservation of olivine, which is unstable in aqueous conditions, indicates that (i) significant subsurface weathering did not occur in this region, despite the potential for liquid water to be present and stable at the temperatures expected at these depths, and (ii) significant surface weathering has not occurred since this layer was exposed.
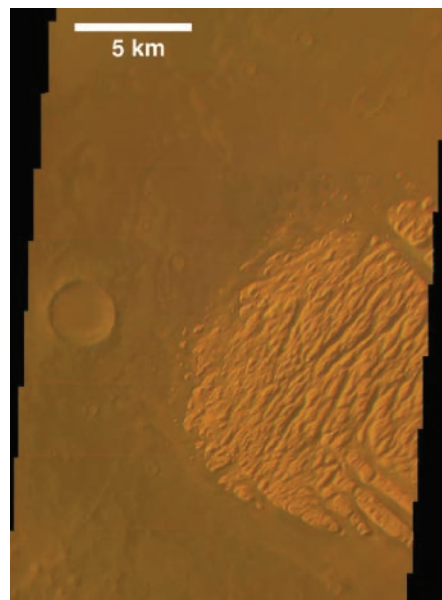

Fig. 7. THEMIS visible camera image of "White Rock" in Pollack crater [2x summing mode; 0.650, 0.540, 0.425 μm bands used for red-green-blue (RGB)]. Image V03233002 centered near 7.9°S, 24.9°E. North is toward the top.

Polar observations. THEMIS has thus far observed the formation of the seasonal cap in the south and the recession of the seasonal cap in the north (Ls 330° to 80°) (*27*). There are temperature patterns in the north polar night that have no corresponding visual or thermal features that can be seen after the sun rises in the spring. In places, during times of low sun angles, temperature patterns similar to thin-layer convection cells with lateral scales of 4 to 20 km are seen; these temperatures are too warm for solid CO_2 and indicate H_2O condensation at 160 to 180 K, corresponding to water vapor mixing ratios of order 10^{-5}.

As the seasonal CO_2 cap recedes in northern spring, visibly bright outliers are left behind that last for days to months. Although the persistent outliers are known to be H_2O, THEMIS can readily distinguish between CO_2 and H_2O frosts to subkilometer scale by temperature, a distinction that has not been possible from visible images. The distribution of small temporal H_2O frost patches is irregular; some bright patches recur annually and some are sporadic (based on previous imaging data). Because the dominant process in the polar night is buffering of low temperatures by CO_2 condensation, winter H_2O accumulation is expected to be quite uniform over longitude and slowly varying with latitude (SOM Text). Thus, the source of these seasonal water frost patches must be local, near the surface, and active on an annual basis.

Morphology and visible color. The visible imager has obtained information on the color properties of the surface and of atmospheric aerosols at the highest spatial resolution yet obtained from Mars orbit (SOM Text). An approximately true color visible image of the relatively bright enigmatic feature known as "White Rock" in Pollack crater (8°S, 25°E) (Fig. 7) indicates that White Rock is actually quite red, consistent with previous lower-resolution Viking color imaging of this feature (*28*). Indeed, the actual color and reflectivity of White Rock is comparable to that of typical bright dusty regions on Mars, suggesting that it is either mantled by thin ferric-rich aeolian dust deposits or consists of weathered or coated ferric materials. The overall rugged morphology and cliff-forming nature of the feature suggest a competent, possibly indurated, substrate or deposit, yet there is also clear evidence that some material has been eroded from this feature (*29*). These observations, combined with knowledge of the color of this feature, may indicate that White Rock is an indurated and weathered sedimentary deposit, perhaps deriving some of its resistance to erosion from cementation by fine-grained ferric oxides. Similar "white" and apparently indurated material was seen at the Mars Pathfinder

landing site (*30, 31*) and was found to be compositionally similar to the surrounding bright drift deposits.

Hydrothermal activity. A major goal of the THEMIS investigation has been the search for evidence of recent geothermal activity. Thermal variations are large, complex, and widespread, complicating simple, algorithmic approaches for detecting anomalous hot or cold regions. In addition, some surfaces where geothermal or hydrothermal activity might be expected, such as in relatively young volcanic fissures or exposed layers in cliff walls, are places where high rock abundances produce the most significant temperature anomalies. To date, however, no temperatures have been identified that cannot be attributed to thermophysical properties (e.g., bedrock or dust exposures) alone.

References and Notes

1. P. R. Christensen *et al.*, *Space Science Reviews*, in press.
2. M. C. Malin, K. S. Edgett, *Science* **290**, 1927 (2000).
3. M. C. Malin, K. S. Edgett, *J. Geophys. Res.* **106**, 23429 (2001).
4. All infrared images presented here were acquired using Band 9 centered at 12.6 μm and are 32 km wide unless otherwise noted.
5. H. H. Kieffer, *Science* **194**, 1344 (1976).
6. H. H. Kieffer *et al.*, *J. Geophys. Res.* **82**, 4249 (1977).
7. M. T. Mellon, B. M. Jakosky, H. H. Kieffer, P. R. Christensen, *Icarus* **148**, 437 (2000).
8. B. M. Jakosky *et al.*, *J. Geophys. Res.* **105**, 9643 (2000).
9. R. E. Arvidson *et al.*, *J. Geophys. Res.*, in press.
10. P. R. Christensen, M. C. Malin, R. V. Morris, J. L. Bandfield, M. D. Lane, *J. Geophys. Res.* **106**, 23873 (2001).
11. M. A. Presley, P. R. Christensen, *J. Geophys. Res.* **102**, 6651 (1997).
12. P. R. Christensen, *Icarus* **68**, 217 (1986).
13. M. D. Lane, R. V. Morris, P. R. Christensen, S. A. Mertzman, *J. Geophys. Res.* **107**, DOI10.1029/2001JE001832 (2002).
14. A. H. Treiman, D. J. Lindstrom, *J. Geophys. Res.* **102**, 9153 (1997).
15. D. M. Burr, A. S. McEwen, S. E. H. Sakimoto, *Geophys. Res. Lett.* **29**, 4 (2002).
16. Rocks greater than ~30 cm in diameter are ~40 K warmer at night than materials with a Mars average thermal inertia. Smaller rocks approach the temperature of particulate material and require proportionately higher abundances to account for the observed temperature increases.
17. R. Sullivan, P. Thomas, J. Veverka, M. Malin, K. S. Edgett, *J. Geophys. Res.* **106**, 23607 (2001).
18. M. H. Carr *et al.*, *J. Geophys. Res.* **91**, 3533 (1977).
19. P. Mouginis-Mark, *J. Geophys. Res.* **84**, 8011 (1979).
20. R. W. Shorthill, *The Moon* **7**, 22 (1973).
21. F. D. Palluconi, H. H. Kieffer, *Icarus* **45**, 415 (1981).
22. P. R. Christensen, H. J. Moore, in *Mars*, H. H. Kieffer, B. M. Jakosky, C. W. Snyder, M. S. Matthews, Eds. (University of Arizona Press, Tucson, AZ, 1992), pp. 686–729.
23. P. R. Christensen, J. L. Bandfield, M. D. Smith, V. E. Hamilton, R. N. Clark, *J. Geophys. Res.* **105**, 9609 (2000).
24. J. L. Bandfield, V. E. Hamilton, P. R. Christensen, *Science* **287**, 1626 (2000).
25. J. L. Bandfield, *J. Geophys. Res.* **107**, 10.1029/2001JE001510 (2002).
26. S. W. Ruff, P. R. Christensen, *J. Geophys. Res.* **107**, 10.1029/2001JE001580 (2002).

27. T. N. Titus, H. H. Kieffer, P. R. Christensen, *Science* **299**, 1048 (2002).
28. S. H. Williams, J. R. Zimbelman, *Geology* **22**, 107 (1994).
29. S. W. Ruff *et al.*, *J. Geophys. Res.* **106**, 23921 (2001).
30. H. Y. McSween Jr. *et al.*, *J. Geophys. Res.* **104**, 8679 (1999).
31. J. F. Bell III *et al.*, *J. Geophys. Res* **105**, 1721 (2000).
32. A. R. Gillespie, A. B. Kahle, R. E. Walker, *Remote Sensing Environ.* **20**, 209 (1986).
33. We would like to sincerely thank all those at Raytheon Santa Barbara Remote Sensing who built the THEMIS instrument, and those at the NASA Jet Propulsion Laboratory, Lockheed Martin Astronautics, and Arizona State University, who built and operate the Odyssey spacecraft. This work was supported by the NASA Mars Odyssey Flight Project.

Myosin V Walks Hand-Over-Hand: Single Fluorophore Imaging with 1.5-nm Localization

Ahmet Yildiz,[1] Joseph N. Forkey,[3] Sean A. McKinney,[1,2] Taekjip Ha,[1,2] Yale E. Goldman,[3] Paul R. Selvin[1,2]*

Myosin V is a dimeric molecular motor that moves processively on actin, with the center of mass moving ~37 nanometers for each adenosine triphosphate hydrolyzed. We have labeled myosin V with a single fluorophore at different positions in the light-chain domain and measured the step size with a standard deviation of <1.5 nanometers, with 0.5-second temporal resolution, and observation times of minutes. The step size alternates between 37 + 2x nm and 37 − 2x, where x is the distance along the direction of motion between the dye and the midpoint between the two heads. These results strongly support a hand-over-hand model of motility, not an inchworm model.

Myosin V is a cargo-carrying processive motor that takes ~37-nm center of mass steps along actin filaments (*1–3*). Defects in this protein lead to immunological and neurological diseases (*4*). Like many other processive motors, it has two heads held together by a coiled-coil stalk (Fig. 1). Each head of myosin V contains a catalytic domain responsible for actin binding and ATP hydrolysis and a light chain–binding domain that likely acts as a lever arm to amplify small nucleotide-dependent conformational changes in the catalytic domain (*3, 5, 6*).
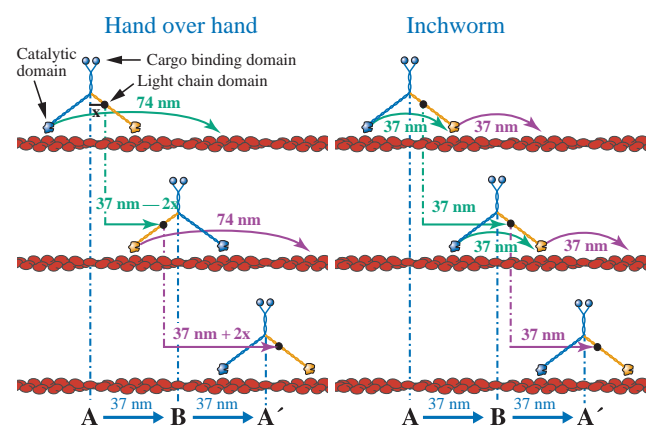
How the two heads of myosin V are coordinated to produce steps is a central, unresolved question. Biochemical and biophysical studies (*3, 6, 7*) suggest a hand-over-hand "walking" model in which the two heads alternate in the lead (Fig. 1, left). Another possibility is the so-called "inchworm" model in which one head always leads (Fig. 1, right). A biophysical study of kinesin, another processive motor, concluded an inchworm model was more likely, although it could not rule out an asymmetric type hand-over-hand mechanism (*8*).

The hand-over-hand and inchworm models make different, testable predictions for the motions of each individual head (Fig. 1). For example, the inchworm model predicts that the

step size of each catalytic domain is equal to the step size of the stalk [35 to 40 nm (*9, 10*) or ~37 nm]. In contrast, the hand-over-hand model predicts that the trailing catalytic domain takes a step that is twice the step size of the stalk while the leading catalytic domain does not move. For a single fluorophore attached to the light chain domain of myosin V, the inchworm model predicts a uniform step size of 37 nm, whereas the hand-over-hand model predicts alternating steps of 37 − 2x, 37 + 2x, where x is the in-plane distance of the dye from the midpoint of the myosin (Fig. 1).

To test these models, we have developed a single molecule fluorescence imaging technique

capable of locating a single molecule in two dimensions to within 1.5 nm, with subsecond temporal resolution and with a photostability that allows observation for several minutes. Total internal reflection epifluorescence microscopy (TIRF) (*11–13*) was used to excite and image many individual fluorophores onto a slow-scan back-thinned charge-coupled device (CCD) with frame-transfer capability, enabling acquisition of multiple sequential images with no interframe deadtime (*14*). Our technique [fluorescence imaging with one-nanometer accuracy (FIONA)] is a 20-fold improvement in the localization accuracy of single fluorophores at room temperature using wide-field methods (*15, 16*) and a ~10-fold improvement in photostability. Scanning confocal microscopy methods using two nanocrystals of different emission wavelengths have previously achieved a precision of ±6 nm with a total integration time of 20 s (*17*). Fluorescence (*18*) and scattering (*19*) from large (30 and 150 nm, respectively) beads have achieved ~2-nm localization within unspecified time resolution and 30 ms, respectively.

FIONA. A single fluorescent molecule forms a diffraction-limited image of width ≈ $\lambda/2$ N.A., or ≈ 250 nm for visible light, where N.A. is the numerical aperture of the collection lens. The center of the image, which, under appropriate conditions, corresponds to the position of the dye, can be located to arbitrarily high precision by collecting a sufficient number of photons. Our method for determining the center relies on

[1]Center for Biophysics and Computational Biology, [2]Physics Department, University of Illinois, Urbana-Champaign, IL 61801, USA. [3]University of Pennsylvania, Pennsylvania Muscle Institute, Philadelphia, PA 19104, USA.

*To whom correspondence should be addressed. E-mail: selvin@uiuc.edu

Fig. 1. Hand-over-hand versus inchworm model of myosin V motility. A calmodulin light chain is labeled with a single fluorescent dye and exchanged into the myosin V light chain domain, where it binds in one of several possible positions (black dot, schematic representation of dye position). In the hand-over-hand model, the rear head moves 74-nm forward but the front head does not move, the stalk moves 37 nm, and the dye takes alternating 37 ± 2x nm steps. (If the dye is a different distance from the stalk in the forward versus rear light chain domains, due to asymmetry in the myosin V structure, then x is the average distance of the dye from the stalk.) In the inchworm model, all parts of the myosin move 37-nm forward, and one head always leads. Adapted with permission from (*32*).